

Analysis of the Cause of High External Q Modes in the JLab High Gradient Prototype Cryomodule *Renascence*

Z. Li, V. Akcelik, L. Xiao, L. Lee, C. Ng, and K. Ko, SLAC, Menlo Park, CA, USA
H. Wang, F. Marhauser, J. Sekutowicz, C. Reece, and R. Rimmer, TJNAF, Newport News, VA, USA

1. INTRODUCTION

The *Renascence* cryomodule [1] installed in CEBAF in 2007 consists of 8 cavities as shown in Figure 1. The first three cavities (#1-#3) in the upstream end are of the Low Loss (LL) shape design, and the remaining 5 cavities (#4-#8) on the beam downstream end are the High Gradient (HG) shape design. The fundamental power couplers (FPCs) are the rectangular waveguides, and the little cylindrical structures are the HOM couplers. The locations of the FPC in the last four cavities are mirrored about the beam z axis. Cavities #4 and #5 form a back-to-back cavity pair. Among the HG cavities installed in the *Renascence* cryomodule, the only identifiable difference from their fabrication documentation is that cavity #5 received an extra EBW pass on one equator weld, specifically cell 5. The non-uniform mechanical tuning required to compensate the fundamental mode tune and flatness for the extra shrinkage of this cell is believed to contribute the most significant differences from the other HG cavities.



Figure 1: Eight cavities in the *Renascence* cryomodule. The first three are the Low Loss shape design and the remaining five are the High Gradient shape design. The locations of FPC couplers are mirrored about the middle of the cryomodule. Cavity 4 and 5 forms a back-back cavity pair. There are concerns of possible trapped modes in the FPC region.

Beam based instability studies on this cryomodule in CEBAF have shown a significant beam breakup (BBU) threshold current reduction, well below design value. Frequency spectrum peaked by the off-sided beam power indicated the cause is due to abnormal high Q modes in the cavity #5. Measured beam off-axis position at the cavity #5 does not correspond to the shunt impedances calculated for an ideal cavity. Low power RF measurements have identified that the problematic modes are in the second dipole band (TM₁₁₀ like). Three of the modes have external Qs two orders magnitude higher than the others, while the rest of modes in the first two dipole bands are normal in terms of the design values. The cause of this abnormality and the future impact on the BBU was not able to be resolved due to the limitations of information that can be obtained from the measurements. It is important to understand the cause of this abnormality so that effective QA/QC measures can be implemented to avoid such problem in the final upgrade design and manufacture.

The goal of this work is to utilize advanced simulation tools to understand the high external Q (Q_{ext}) problem observed in the *Renascence* cryomodule. In the past years, SLAC has built a set of state-of-the-art advanced simulation tools based on finite-element unstructured meshes and parallel computation implementations on supercomputers [2, 3]. The codes are capable of simulating large complex RF systems with unprecedented resolution and turnaround time. They have been successfully applied to many existing

and future accelerator R&D projects to improve the machine performance and to optimize the designs. These tools are essential to perform accurate full system analyses such as the JLab's SRF cavities. We will use the simulation results and the data from the RF measurements to gain a better understanding of the cavity performance and tolerance issues and provide a solid foundation to do the BBU simulation and prediction for the 12GeV Upgrade project by using JLab's BBU codes.

In this report, we will focus on the following two main tasks:

1) Ideal cavity simulation – to evaluate the effectiveness of the damping by the higher-order-mode (HOM) couplers, and search for possible trapped modes in a back-to-back cavity pair (e.g. cavity #4 & #5).

2) Abnormal cavity study – to understand the cause of the high Q_{ext} modes in cavity #5 using an advanced Shape Determination Tool.

2. The HG Cavity Model

CAD model of the High Gradient cavity generated by IDEALS at JLab was not fully compatible with the meshing software CUBIT, which is used to generate the finite element meshes for the eigensolver Omega3P. The solid model was re-built from the SuperFish input file (for the 7-cells) and the HOM coupler's 2D drawings. The new model was compared with the original JLab model to assure that the dimensions and coupler locations are accurate. The Field Probe (FP) is not included in the CUBIT model since it does not affect the RF parameters. The JLab's model (top) and the CUBIT model of the HG cavity are shown in Figure 2.

There are two HOM couplers on each end of the cavity. The FPC end HOM couplers have the pickup probes removed due to coupler heating problems [4]. The HOM is only damped by two couplers at the FP end. The coupler loop and pickup details are shown in Figure 2 (bottom).

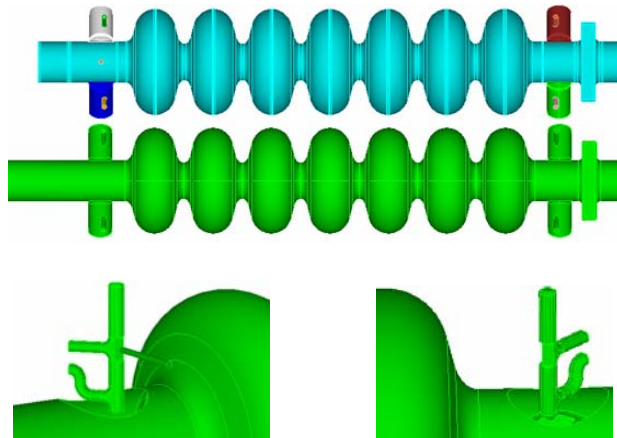


Figure 2: The 7-cell High Gradient (HG) cavity model. Top: JLab model; Middle: CUBIT model for Omega3P simulation; Bottom: HOM details. The FPC side HOM pickup ports are blanked off, no pickup probes for HOM (right figure). Only the HOM couplers on the opposite side of the FPC have pickup probes for HOM damping (left figure).

3. HOM Damping Of a Back-to-back HG Cavity Pair

3.1 Simulation model



Figure 3: The back-to-back cavity pair (half model) used in simulation to study the HOM damping.

The back-to-back cavity pair as shown in Figure 3 was simulated to study the effectiveness of HOM damping by the HOM couplers. The cavities have a two-fold symmetry about the horizontal plane. Only half of the geometry is needed for the computational model. To further reduce the problem size, only one of the cavities in the cavity pair will be simulated to take advantage of mirror symmetry about the middle plane between the FPC couplers. Different colors in the model indicate regions that will require different mesh densities in order to optimize the simulation accuracy and the use of computing resources. The convergence on mesh quality was studied. Figure 4 shows a typical mesh used for the calculation where the geometry details in the HOM coupler region (yellow color) is modeled with locally refined mesh. This kind of adaptive mesh generation is a big advantage of the unstructured and conformal finite element scheme. The eigensolver Omega3P utilizes higher-order interpolation functions for the fields and higher-order surfaces representations for the geometry, further enhancing the computing accuracy.

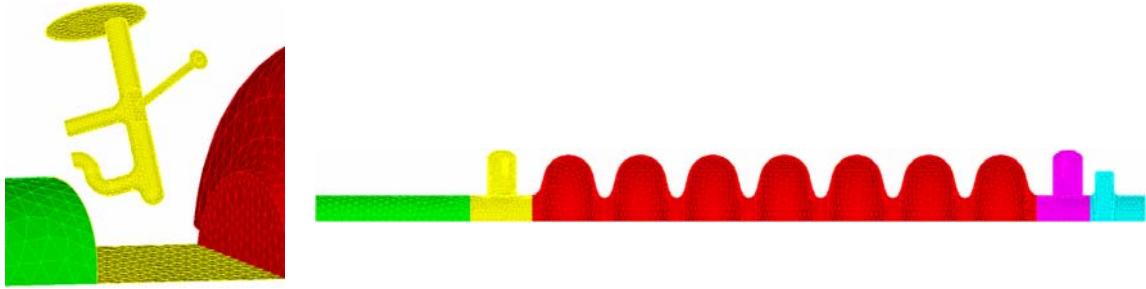


Figure 4: Finite element meshing is used for simulating the 7-cell high-gradient cavity. The locally refined meshes in the HOM coupler region (yellow color) are shown on the left.

3.2 Monopole operating mode and field flatness

The cavity dimensions provided in the SuperFish file are room temperature values. With these dimensions, the TM010 π mode is 1495-MHz. In order to compare with the measurement data, the Omega3P model was scaled to the cold temperature dimensions. With the “cold” model, the frequency of the TM010 π mode is 1497-MHz, and the E_z field distribution is flat from cell to cell as shown in Figure 5.

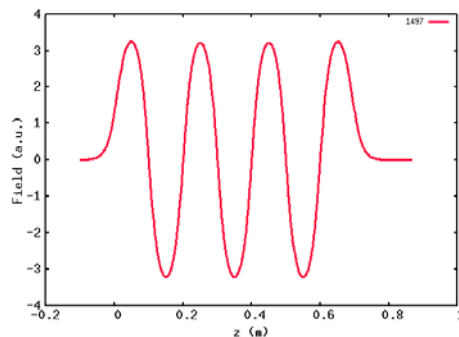


Figure 5: The E_z field distribution of TM010 π mode along the beam axis.

3.3 Dipole modes in the structure

The frequencies of the vertical polarization modes of the first three dipole bands are listed in Table 1. There are 9 modes in the first dipole band and 7 modes in each of the second and the third dipole bands. Two additional modes in the first band are due to the coupling of the $3\pi/7$ mode to the HOM couplers. The mode patterns of these modes are shown in Figure 6. The first and the second band dipole modes are below the beam pipe (35-mm radius) TE11 cutoff frequency of 2.51 GHz and are localized in the 7-cells. The

third band modes are above the beam pipe cutoff, and may form coupled modes between cavities.

Table 1: Frequencies (in MHz) of the vertical polarization modes of the first three dipole bands.

1st Band	2nd Band	3rd Band
1883.2	2063.5	2859.6
1894.1	2135.1	2889.6
1905.7	2146.2	2924.7
1912.6	2154.2	2958.5
1917.1	2159.1	2986.4
1944.9	2161.6	3005.5
1980.7	2162.7	3019.9
2018.7	2178.4 (trapped)	
2053.5	2186.8 (trapped)	

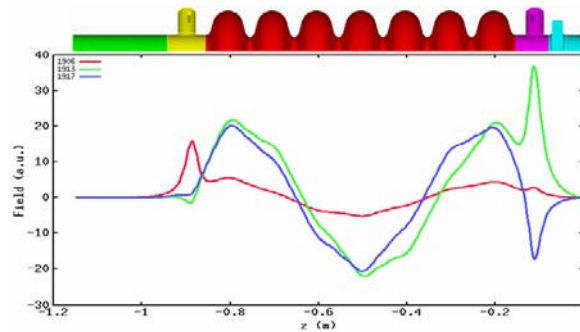


Figure 6: The $3\pi/7$ mode in the first dipole band coupling to the HOM couplers results in two additional dipole modes in the 7-cell HG cavity. This picture shows the mode patterns of the three coupled modes (F=1905, 1912, 1917 MHz).

3.4 HOM damping

The HOM damping was calculated using the half-geometry as shown in Figure 4. The magnetic and electric boundary conditions were used respectively on the beam pipe symmetry plane on the FPC side to simulate the “even” and “odd” modes in a cavity pair. The FPC port was closed with a magnetic boundary. The damping of the first two dipole bands in the vertical plane is not affected by this boundary termination since the modes’ frequencies are below the TE₂₀ cutoff of the FPC waveguide. The FPC coupler may contribute additional damping to the horizontal dipole modes and higher-band vertical modes. The Q_{ext} results shown here include only the damping effect due to the HOM couplers.

The Q_{ext} and the transverse impedance calculated for the first three dipole bands are shown in Figure 7 and 8 respectively. The beam pipe symmetry boundary conditions have little effects on the damping of the first two dipole band modes. They do have some effects on the third band modes since they are above the beam pipe cutoff and could couple to adjacent cavities through the beam pipe. The Q_{ext} s are generally below 10^5 for the first and third dipole band modes, in low 10^6 for the second dipole band except for one of the low $(R/Q)_T$ modes which is above 3×10^7 . As mentioned above, the Q_{ext} s for the horizontal modes (h-mode) do not include the damping due to the FPC. There is certain asymmetry in damping for the vertical and horizontal modes, which can be minimized by adjusting the coupler orientations. For the modes of the third dipole band, both horizontal and vertical polarizations are above the cutoff of the FPC waveguide (TE₂₀ for vertical

and TE₁₀ for horizontal). It is expected that the Q_{ext} s of these modes in an actual cavity would be lower than those shown in Figure 7. In addition, the third band modes also propagate in the 35 mm radius beam pipe, as shown in Figure 9. The damping by the HOM coupler may depend on the mode patterns formed in the beam pipe regions due to the reflections from the adjacent cavities. The shunt impedance values shown in Figure 8 are per cavity, except for the FPC trapped modes that are for the cavity pair. Because of the cavity to cavity coupling for the third band modes, the shunt impedance values of a cavity pair may vary depending on the coupling. Table 3 is a summary of the RF parameters of the first three dipole bands.

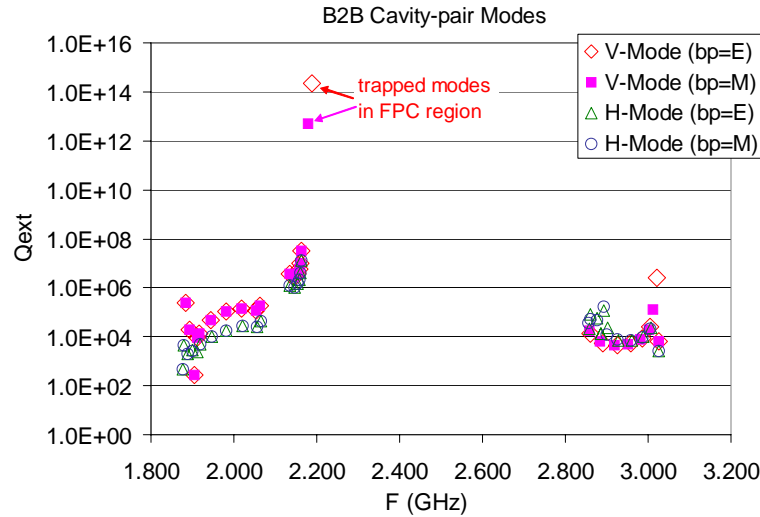


Figure 7: The Q_{ext} s of the first three dipole bands in a back-back cavity pair of the High Gradient cavity. The Q_{ext} s are only due to the HOM couplers. There are two possible trapped modes in the FPC region in the vertical polarization.

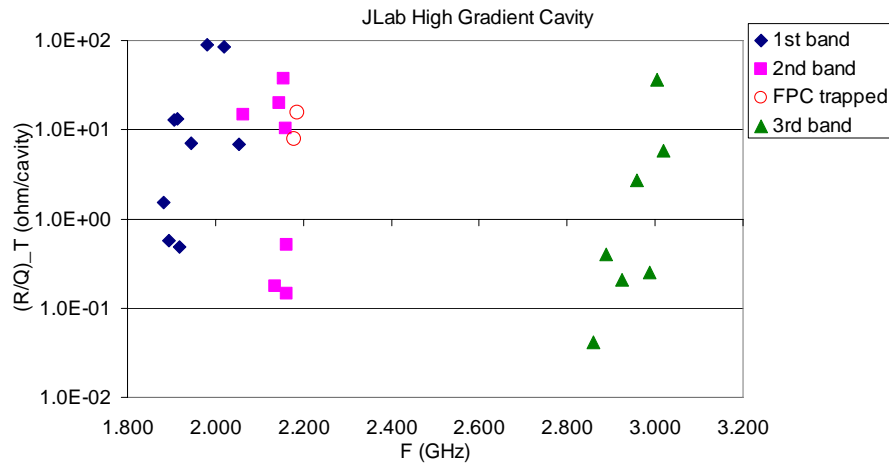


Figure 8: Transverse shunt impedances of the vertical modes in the High Gradient cavity. The hollow dots are the trapped modes in the FPC region. The shunt impedance values of the trapped modes are for a cavity pair.

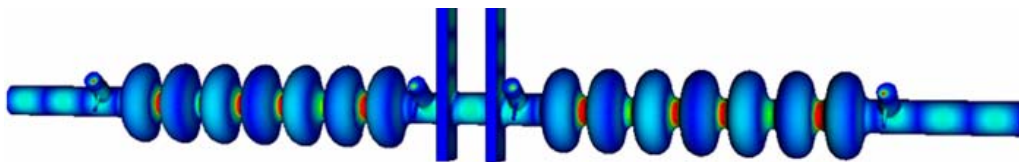


Figure 9: A mode in the third dipole band couples to the adjacent cavities through the beam pipe. Electric boundary conditions were applied at the beam pipe end. The Q_{ext} will vary depending on the effective boundary due to the adjacent cavity.

Table 3: HOM R/Q_T and Q_{ext} including trapped modes in the HG cavity

Freq (GHz)	R/Q _T (Ω/cavity)	Q _{ext}
1.88324	1.53	2.37E+05
1.89410	0.58	1.95E+04
1.90569	12.96	2.79E+02
1.91258	13.38	9.18E+03
1.91714	0.48	1.31E+04
1.94487	6.99	4.90E+04
1.98071	89.18	1.04E+05
2.01870	85.02	1.46E+05
2.05347	6.92	1.23E+05
2.06348	14.74	1.87E+05
2.13512	0.17	3.73E+06
2.14622	19.97	2.91E+06
2.15424	37.26	3.74E+06
2.15905	10.26	5.59E+06
2.16161	0.15	9.95E+06
2.16274	0.51	3.17E+07
2.17843	15.68	trapped
2.18677	31.36	trapped
2.85964	0.04	1.38E+04
2.88961	0.40	5.64E+03
2.92470	0.21	4.44E+03
2.95848	2.68	5.24E+03
2.98641	0.25	8.87E+03
3.00550	36.06	2.48E+04
3.01989	5.88	2.48E+06

3.5 Possible trapped modes in the FPC region

There are two possible trapped modes found in the FPC region in the vertical plane as shown in Figure 10 in a back-to-back cavity pair configuration. The frequencies of these two modes are 2.178 GHz and 2.187 GHz and with (R/Q)_T of 16 Ω/pair and 31 Ω /pair respectively.

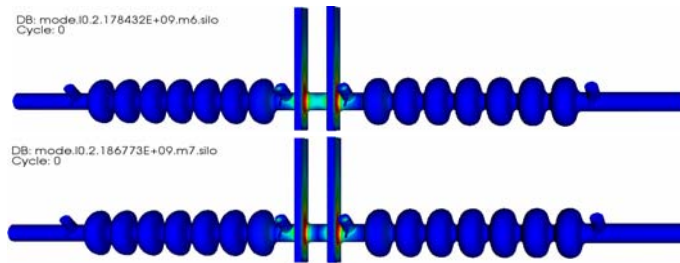


Figure 10: Possible trapped modes in the FPC region of the cavity pair. These modes have large shunt impedances.

The trapped modes do not couple to the HOM couplers that are located on the opposite end of the FPC coupler. They do couple to the TE₂₀ modes of the FPC waveguide. However, the cutoff frequency of the TE₂₀ mode in the FPC waveguide is around 2.2 GHz. In the ideal case, these modes will not leak out from the FPC coupler. However the long evanescent tails of the modes (since frequencies so close to cutoff) may result in losses to the warm region of the FPC coupler and lower the Q. The RF measurements from the FPC coupler will not be able to pickup signals from these modes even though

they may have low Q. In reality, any transition of the FPC coupler or imperfection of geometry may convert (partially) the TE₂₀ mode into TE₁₀ mode, resulting in additional damping (in such a case, one would be able to observe these modes in the RF measurements from the FPC).

3.6 HOM damping with FPC side of HOM coupler cans removed

The HOM couplers on the FPC side were blanked out in the *Renascence* prototype cavities due to RF heating considerations [4]. So the HOMs were not damped by these couplers at all. In the future cavities (like in the C100 cryomodule), these HOM couplers will be completely removed to save cost [5]. As a confirmation evaluation, we simulated the simplified version of the high gradient cavity. There are no significant differences in Q_{ext} as shown in Figure 12. The possible FPC trapped modes still exist at around 2.18 GHz.

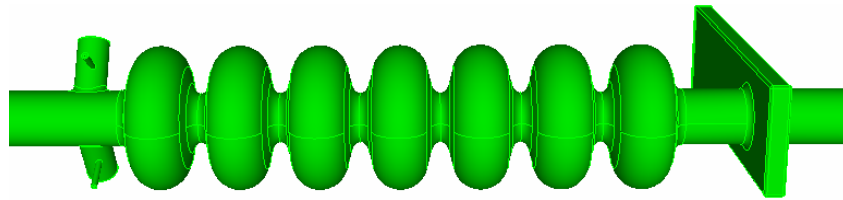


Figure 11: Modified version of the HG cavity with the FPC side HOM couplers removed.

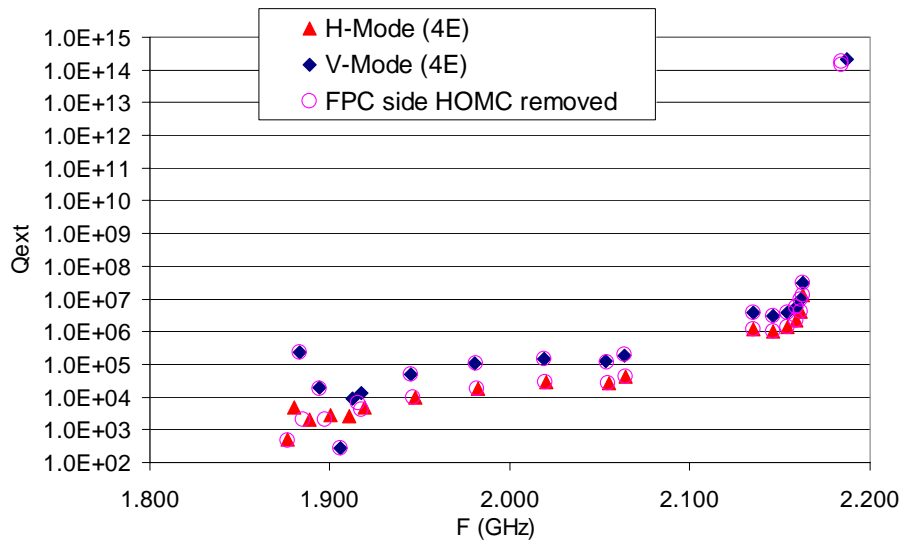


Figure 12: Comparison of HOM damping between the original (Figure 2) and modified (Figure 11) designs.

4. Shape Determination of the Abnormal HG Cavity #5

4.1 Abnormality of cavity #5

The HOM measurement results of the five High Gradient cavities in the *Renascence* Cryomodule (installed in zone NL04 of CEBAF) are plotted in Figure 13. The hollow circles and squares are the Omega3P calculations for comparison. The measured values showed typical scattering around the ideal cavity (Omega3P calculations) due to fabrication errors. However, an abnormality was found in cavity #5 where the Q_{ext} s of three modes in the second dipole band are more than one order of magnitude higher than those of the cavities #4, #6, #7 and #8. These modes are the $4\pi/7$, $5\pi/7$ and $6\pi/7$ modes

that are high in $(R/Q)_T$. As a result, CEBAF encountered two of these three modes causing BBU threshold current significantly lowered than normal operation values.

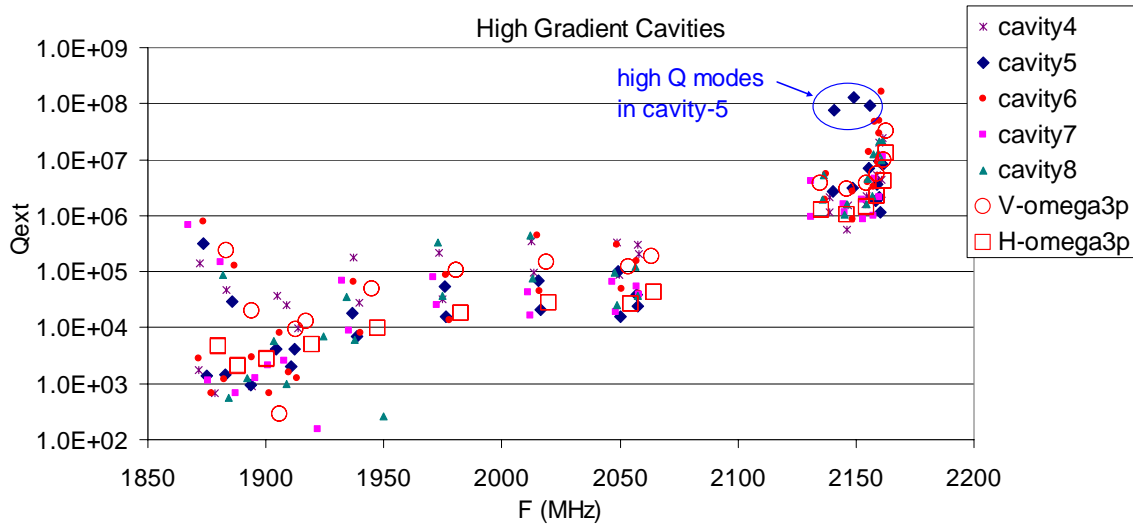


Figure 13: Measured loaded Q on the HG cavities in JLab’s *Renascence* cryomodule and comparison with Omega3P simulation result. V: vertical polarization; H: horizontal polarization.

What is mysterious about the abnormality in cavity #5 is that only these three of all the first two band modes are high in Q_{ext} , while the rest of the dipole modes in this cavity have comparable Q_{ext} as the other cavities. This suggests that the HOM couplers are not likely the cause, rather there might be distortions in the cavity body that caused significant tilt to the fields of these three modes toward the FPC side of the cavity, while the rest of the modes are less affected.

Studies on the sensitivity of Q_{ext} to the cell imperfections were performed. It was found that it is hard to reproduce the abnormal high Q_{ext} in cavity #5 via just a simple shape distortion. Thus, a more complicated combination of multi-cell imperfections was required. Because of the nonlinear dependence of RF parameters on the cavity shape distortions, an advanced tool is needed to tackle such a problem.

4.2 Comprehensive Shape Determination Tools

As it is known that the effects of shape deviation of the real cavity from the design shape may result in significant impact on cavity RF parameters. However, most of these shape deviations are unknown in the final cavity installation because of the complicated process of assembly and tuning. Being able to resemble the shape distortion using measurable RF quantities such as cavity frequencies and Q_{ext} s will provide valuable information for the cavity design and the quality assurance in manufacture and to improve cavity performance. SLAC’s Shape Determination Tools were developed to perform such an analysis.

The Shape Determination Tools reproduce the unknown shape by solving an inverse problem. The formulation of the inverse problem is based on the least squares minimization of the modeled and recorded response spectra. The goal of the algorithm is to find the best shape that minimizes the least squares misfit between the measured and simulation models. The shape perturbations in the simulation model are parameterized using predefined geometry parameters. The inversion of the problem quantifies these parameters to determine the cavity true shape.

The nonlinear least squares problem is solved using the Gauss-Newton method. An adjoint method was developed and implemented in the code to compute the design

sensitivities, e.g. sensitivity of the shape parameters to the RF quantities. The difficult part in the shape determination problem is that the numerical system is ill-posed and rank deficient. To remedy these difficulties, the truncated SVD technique [6] is employed in the code. In each of the nonlinear iterations, the main computation effort is to solve the complex Maxwell eigenvalue problem and the adjoint problems. The nonlinear algorithm typically converges within a handful of iterations. A more detail description of the shape determination algorithm can be found in Ref. [6].

4.3 Shape Determination for the Abnormal HG Cavity

The parameterization of each single cell of JLab 7-cell HG cavity is shown in Figure 14. There are five sections along the cell profile, dt1 to dt4 and dr, which can be moved in the normal direction of the surface to produce the shape distortion. The range of these segments is about 10-mm along the z-direction. Positive deviations of the profile increase the cavity volume. The iris radius “a” and the cell length “z” are also parameterized that can be adjusted. However the cell iris radii “a” were kept fixed in this study assuming the distortion on the iris is likely to be small.

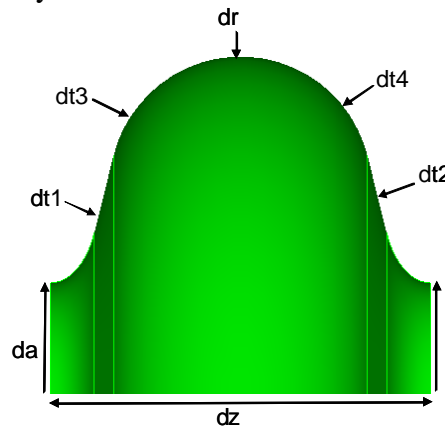


Figure 14: Parameters used in shape determination. Using a different set of parameters may improve solution accuracy.

The goal is to determine the deformed cavity shape using measured frequencies and Q_{ext} values. The measurement data were taken from Ref [7]. The measurable RF parameters used in the shape determination include the 7 monopole frequencies, 12 dipole frequencies and 6 Q_{ext} values as listed in Table 4. The half structure model as shown in Figure 4 was used for the shape determination simulation. At the moment, the shape determination tool can only use the same boundary condition for both the monopole and dipole modes on the symmetry plane, which is magnetic in this case. So only the monopole and the horizontal dipole modes can be calculated. In order to analyze the abnormal high Q_{ext} modes existed in the vertical plane, we assume that the same mode in the horizontal plane will have the same Q_{ext} if the FPC coupler is terminated electrically. We believe that this is a valid assumption, since the deformation being modelled is cylindrically symmetric and the HOM couplers have the same damping for both the vertical and horizontal modes. The fact that there are no abnormal high Q_{ext} modes in the horizontal polarization in cavity #5 might be attributed to the damping due to the FPC coupler when it is open. With this assumption, the dipole frequencies listed in Table 4 are those of the horizontal modes while the Q_{ext} s are those of the corresponding vertical modes. There are a few modes in the first dipole band were not used in the simulation due to difficulties in relating the frequencies and actual modes. The field flatness of the TM010 π mode is also a constraint. The objective of the shape determination is to minimize the weighted least squares misfit of the (“measured” and “computed”) frequencies, Q_{ext} s, and field flatness of the monopole operating mode.

Table 4: Frequency and Q values used in HG cavity shape determination.

	F (MHz)	Q_{ext}
Monopole: These frequencies were from the warm RF measurement. They were scaled to the cold cavity in the simulation, e.g. $F_{\pi}=1497$	1467.082	
	1471.019	
	1476.723	
	1482.939	
	1488.753	
	1492.776	
	1494.230	
1 st band dipole	1910.560	
	1936.439	
	1975.635	
	2015.502	
	2049.119	
2 nd band dipole	2057.033	
	2140.415	7.6e7
	2148.514	1.3e8
	2155.444	9.3e7
	2158.258	3.6e6
	2159.907	1.1e6
	2160.080	8.0e6

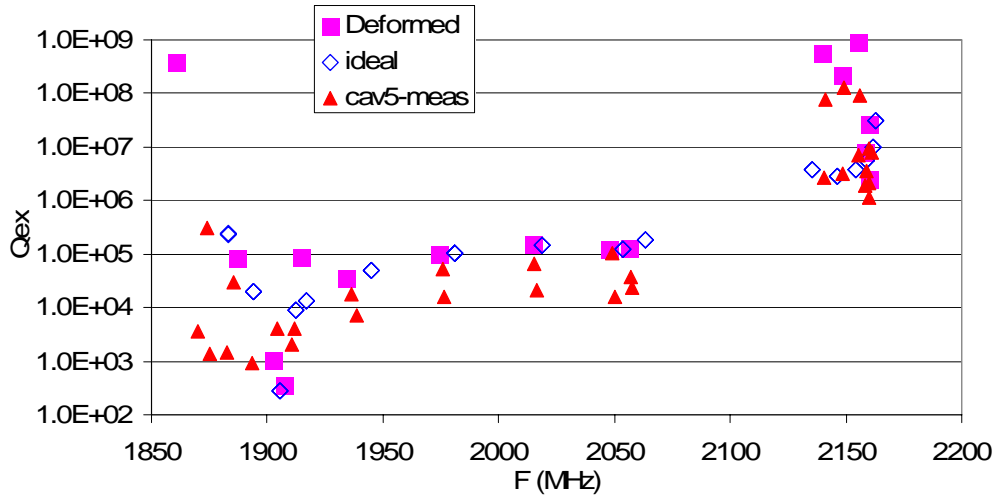


Figure 15: Q_{ext} of the vertical modes for the ideal and deformed cavities.

Figure 15 shows the Q_{ext} result of a deformed cavity using the shape parameters defined in Figure 16. The measured data on cavity #5, triangular dots, and the calculated on deformed cavity, square dots, are in good agreement across the first and second dipole bands. The deformed shape not only reproduced the three high Q_{ext} modes in the second band, it also reproduced the low Q_{ext} s for the modes around 2160 MHz which also agree well with measurement.

On the left of Figure 16 are shown the distortion parameters of the deformed cavity. The resulted profile parameters, $dt1-4$ and dr , in the deformed shape are within a couple of millimeters deviations from the ideal design. Considering that the ranges of the deformations represented by these parameters are small, about 10 mm along the z-axis, the integrated volumes accounted for the effective imperfections in these regions look

quite reasonable. The dominant cavity distortion is the cell length “dz”, the red triangular points. Most of the cells are shorter by 2-3 millimeters. The total length of the deformed 7-cell cavity is about 8.2 mm shorter than the ideal design. This length shortage has been in good confirmation with the cavity #5’s QC data, Ref [8]. As to the individual cells, there were no cell length measurement data available for a detailed comparison. However we have tried to extract the cell length information from the E_z field plot of cavity #5 bead pulling data after the final tuning [9]. We used a “ruler” to measure the node-to-node distance of the E_z^2 profile (obviously not the most accurate means) to obtain the relative cell length distribution. The length of the two end cells cannot be measured because of the evanescent tail. The rough data of the middle 5 cells are in good agreement with the shape determination.

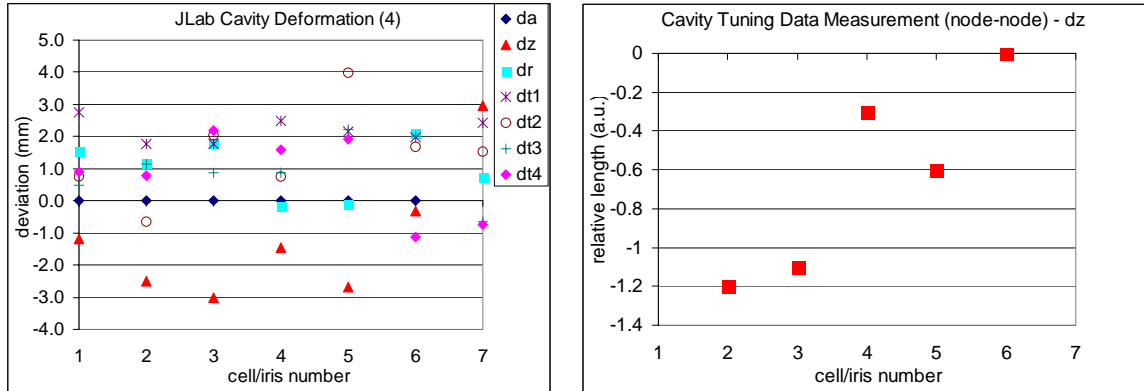


Figure 16: Shape parameters of the deformed HG Cavity #5 shape.

4.4 The field distribution in the deformed cavity

Both the frequency and the E_z field flatness of the operating mode, TM010 π mode, are constraints in the shape determination. So the frequency of 1497 MHz and the flat E_z field is “guaranteed” in the deformed shape.

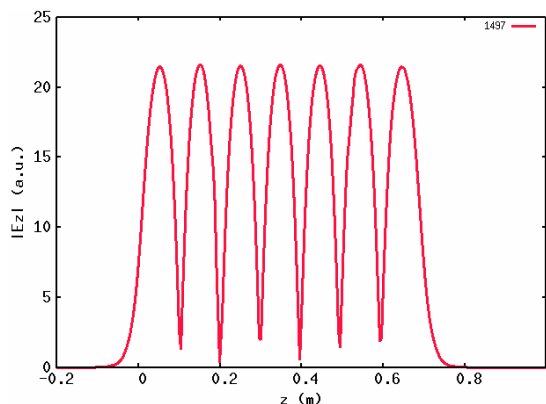


Figure 17: E_z field of TM010 π mode is flat in the deformed cavity

The field distribution of the three abnormal modes in the deformed cavity is significantly different from that in the ideal cavity, Figure 18. In the ideal cavity, the fields are symmetrically distributed through out the cavity. While in the deformed cavity, they are heavily tilted toward the FPC end of the cavity. The fields in the HOM coupler region are more than one order of magnitude lower resulting in ineffective damping.

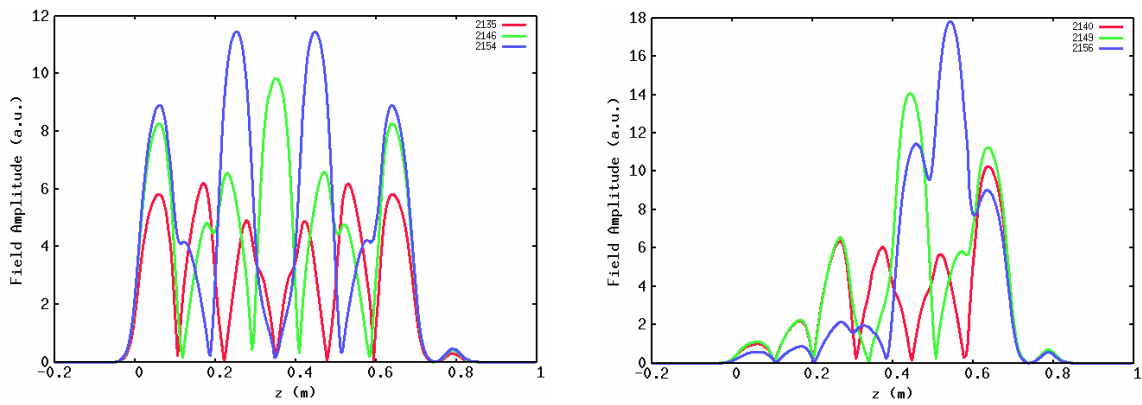


Figure 18: Comparison of the electric field of the abnormal modes. Left) ideal design; Right) deformed cavity with high Q_{ext} modes.

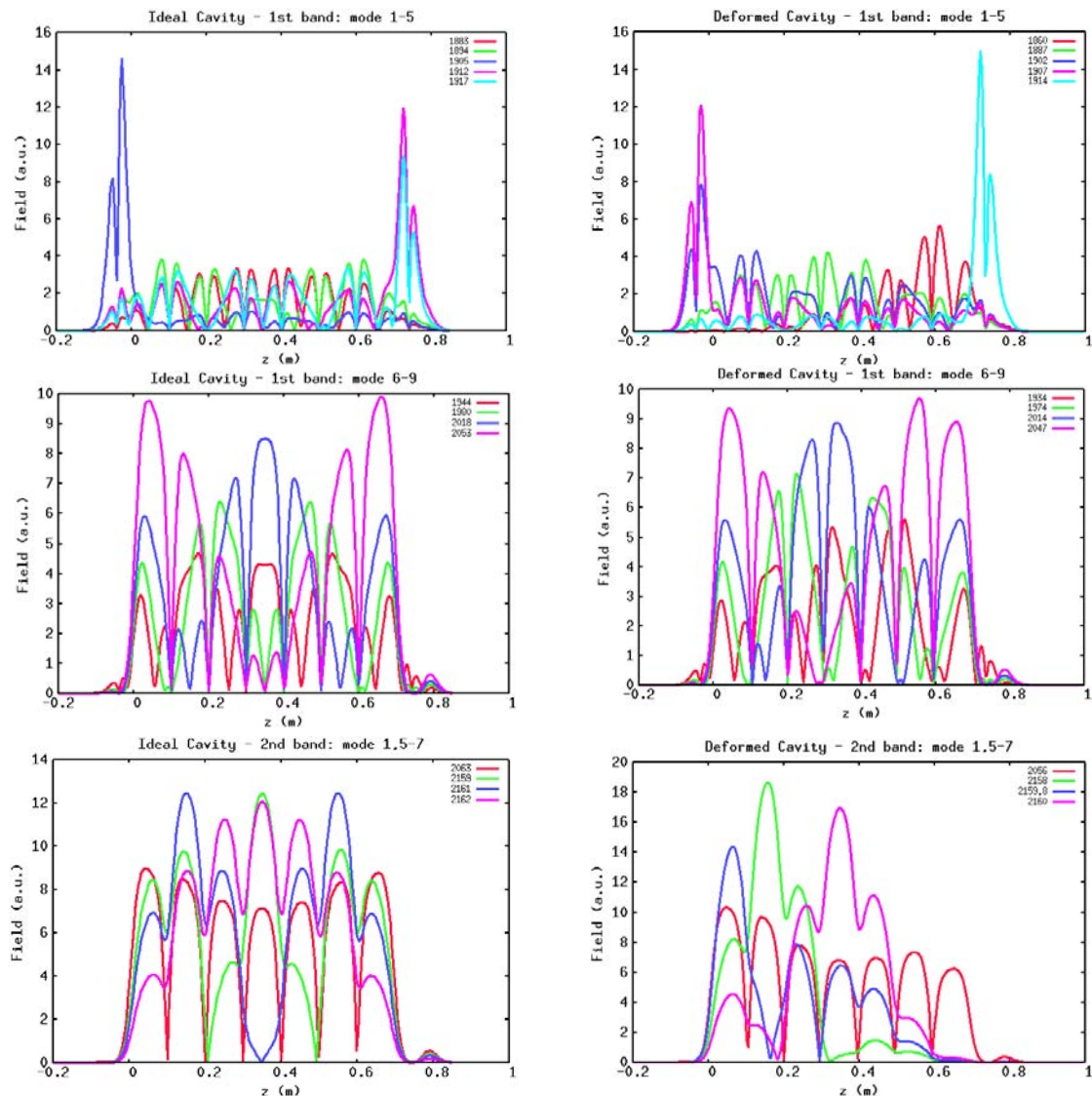


Figure 19: Electric field distributions in an ideal HG cavity (left column) and in a deformed HG cavity (right column). The top and middle rows are for the 1st dipole band modes. The bottom row are for 2nd dipole band normal (or lower, in deformed) Q_{ext} modes.

The field distributions of the remaining first 2 dipole bands are compared in Figure 19. The plots on the left hand side are for the ideal cavity. The top and middle plots are for the 9 modes in the first dipole band. The bottom plot shows the rest of the 4 modes in the second dipole band. Accordingly, the plots on the right hand side are for the deformed cavity. In the first dipole band, there are a couple of low frequency modes that show noticeable shifts in field distribution while most of the modes are not altered as much by the deformation. As a result, the damping Q_{ext} s stayed the similar level as the ideal cavity. The fields of higher frequency modes in the second dipole band are tilted toward the HOM coupler end by the deformation, with one of them of more significant, resulting in lower Q_{ext} .

4.5 Uniqueness of solutions

As mentioned earlier, the formulation of the shape determination problem is based on the least squares minimization of the modeled and deformed response spectra. In most cases the numerical system is ill-posed and rank deficient, depending on the available measured data and the parameters of the cavity distortion used. The solutions of the shape determination system are in general not unique. The result presented above is a solution that takes into account the most of the usable data (data of the identifiable modes in the first two bands) from the measurements and they have the best fit to the important RF parameters. A few other solutions have been obtained with different selections of input data. Although there are certain variations in the resultant shape parameters, all solutions lead to the conclusion that the dominant cavity distortion is the cavity length and the total length is about 8 mm shorter than the ideal design. The predicted deformed cavity length agrees well with the QC measurement of cavity #5 before the string assembly [8]. The 8 mm shortage of cavity length is either due to the e-b welding rework on one of cell's equators or due to the cavity tuning for the fundamental field flatness. The Shape Determination Tools have successfully revealed the dominant cause of the high Q_{ext} abnormally in cavity #5.

5. The Transverse Shunt Impedance

The tilt of the field not only caused the ineffectiveness in damping, but also altered the transverse shunt impedance $(R/Q)_T$ of the modes. Table 5 and Figure 20 show the differences in $(R/Q)_T$ between the ideal and deformed cavities. Among the high Q modes in the second band, the transverse shunt impedance of the $5\pi/7$ mode (2146 MHz in the ideal cavity, 2148 MHz in the deformed cavity) is about $19 \Omega/\text{cavity}$ in both cavities, while the transverse shunt impedance of the $4\pi/7$ mode (2154 MHz in the ideal cavity, 2155 MHz in the deformed cavity) has a significant difference. It is $37.5 \Omega/\text{cavity}$ in the ideal cavity, the highest in the second dipole band, and is $10.5 \Omega/\text{cavity}$ in the deformed cavity, nearly a factor of four lower than the ideal cavity and about half that of the $5\pi/7$ mode. The BBU threshold measured for the $5\pi/7$ mode (2149MHz) is about half of the $4\pi/7$ (2156MHz) mode in the cavity #5 [10], which confirms the ratio of the shunt impedance between the $5\pi/7$ and $4\pi/7$ modes. Notice that in an ideal cavity, the threshold current for the $5\pi/7$ mode (2146MHz) would have been twice as much as the $4\pi/7$ (2154MHz) mode if the beam transfer function and circulation phase are the same.

Table 5: Comparison of transverse shunt impedances between the ideal and deformed cavities.

Ideal Cavity			Deformed Cavity		
F (MHz)	RoQ_T(ohm/cavity)	Qext	F (MHz)	RoQ_T(ohm/cavity)	Qext
1883.24	1.53	2.373E+05	1860.94	5.57	3.762E+08
1894.10	0.58	1.952E+04	1887.04	0.30	8.319E+04
1905.69	12.96	2.793E+02	1902.65	18.86	1.008E+03
1912.58	13.38	9.178E+03	1907.19	3.63	3.582E+02
1917.14	0.48	1.307E+04	1914.64	8.49	8.891E+04
1944.87	6.99	4.903E+04	1933.96	1.22	3.589E+04
1980.71	89.18	1.035E+05	1974.21	65.38	9.942E+04
2018.70	85.02	1.457E+05	2014.48	105.88	1.569E+05
2053.47	6.92	1.226E+05	2047.65	24.72	1.258E+05
2063.48	14.74	1.871E+05	2056.43	10.08	1.293E+05
2135.12	0.17	3.727E+06	2140.07	6.71	5.729E+08
2146.22	19.97	2.907E+06	2148.4	19.17	2.186E+08
2154.24	37.26	3.740E+06	2155.36	10.47	8.926E+08
2159.05	10.26	5.588E+06	2158.18	3.76	8.069E+06
2161.61	0.15	9.954E+06	2159.83	13.07	2.525E+06
2162.74	0.51	3.168E+07	2159.96	1.56	2.604E+07

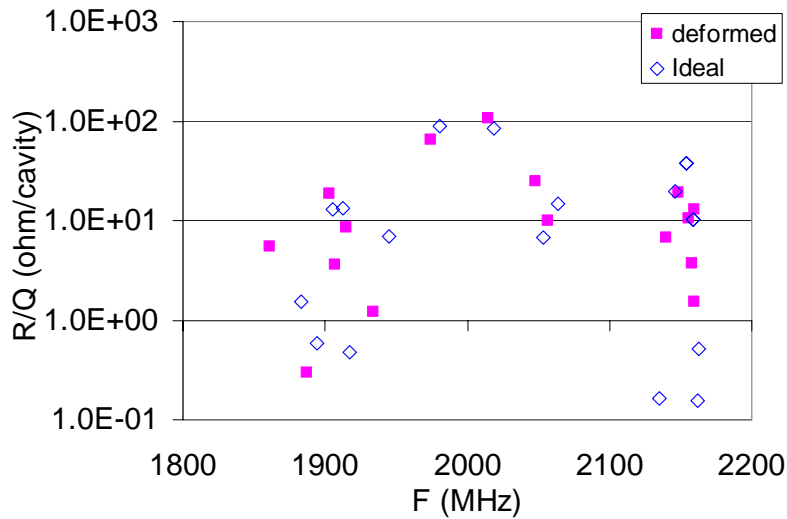


Figure 20: Comparison of transverse shunt impedances between the ideal and deformed cavities.

6. Summary

Using the high performance computing tools developed at SLAC, we were able to search for the trapped modes in the back-to-back High Gradient cavity pair in the JLab *Renascence* prototype cryomodule. The modes were calculated up to the third dipole band. The Q_{ext} s of the first two dipole band modes are in good agreement with the measurement data. Two possible trapped modes were found in the FPC-FPC (horizontal oriented) region of the cavity pair in the vertical plane around 2.18 GHz. These two modes have large shunt impedances and might be harmful to the beam. However, the frequencies of these two modes are very close to the cutoff frequency of the TE₂₀ mode of the FPC coupler. The modes may lose energy due to the long evanescent tail to the warm region of the coupler or due to leakage from possible conversion of TE₂₀ to TE₁₀ by the coupler geometry. These two trapped modes were not found in the cold cryomodule measurement.

The SLAC Shape Determine tools have been successfully used to reproduce the cavity imperfections using the measured RF quantities as the input and to understand the cause of the abnormal high Q_{ext} modes in the cavity #5. The dominant cause was found to be the significant deviations of the cell length from the ideal design. Most of the 7 cells in cavity #5 are shorter by 2-3 mm in length, resulting in a total shortage of the cavity length by about 8 mm, which agrees well with the cavity #5's QC data. This deformation dramatically tilted the fields of some dipole modes in the second band, resulting in high Q_{ext} for three of the passband modes and also causing the shunt impedances to differ from those of the ideal cavity. These tools provided valuable information for the cause of the "after fact" cavity which generated a BBU threshold current lower than predicted value. These computer diagnostic and simulation tools also gave us a lesson to learn that we have to put a quality assurance program in HOM damping performance during the cavity fabrication and tuning processes to confirm the dangerous HOM's field flatness and coupling external Q before the cavity finally installed into the accelerator.

The simulations in this report were performed on the NERSC supercomputers at Lawrence Berkeley National Laboratory.

7. References:

1. E. F. Daly et al., "Improved Prototype Cryomodule for the CEBAF 12 GeV Upgrade," PAC03, p.1377, TPAB077.
2. L.-Q. Lee, et al, "Advancing Computational Science Research for Accelerator Design and Optimization," Proc. of SciDAC 2006 Conference, Denver, Colorado, June 25-29, 2006.
3. C. Ng, et al, "State of the Art in EM Field computation," Proc. EPAC2006, Edinburgh, UK, June 26-30, 2006.
4. C. E. Reece, et al, "Diagnosis, Analysis, and Resolution of Thermal Stability Issues with HOM Couplers on Prototype CEBAF SRF Cavities," SRF 2007, Oct. 15-19, 2007, Beijing, China.
5. C. E. Reece et al., "Optimization of the SRF Cavity Design for the CEBAF 12 GeV Upgrade," *ibid.*
6. V. Akcelik, et al, "Shape Determination for Deformed Electromagnetic Cavities," *Journal of Computational Physics* 227 (2008) 1722–1738.
7. Processed data in JLab's share folder, unpublished.
M:\asd\asddata\BBUatCEBAF\Processed_data\RF\HOMsurvey_processed\All_Cavities_V2008-04-11.xls
8. JLab's NL11 Cavity Sub-assembly Inspection/Acceptance Traveler, C12-REN-CST-CAV-SUB R3-0, SerialNum: HG002, SeqNum: 4.
9. Copy of D. Forehand's bead-pulling data logbook, on Jan. 15, 2005.
10. R. Kazimi et al, "Observation and Mitigation of Multipass BBU in CEBAF" to be published in EPAC 2008 WEPP087 paper ID 4256.